Entangled pairs of 2p atoms produced in photodissociation of H$_2$ and D$_2$

Yutaro Torizuka,[1] Kouichi Hosaka,[1,*] Philipp Schmidt,[2] Takeshi Odagiri,[3] Andre Knie,[2] Arno Ehresmann,[2] Ryoko Kougo,[1] Masashi Kitajima,[1] and Noriyuki Kouchi[1]

[1]*Department of Chemistry, Tokyo Institute of Technology, Meguro-ku, Tokyo 152-8551, Japan*
[2]*Institute of Physics and Center for Interdisciplinary Nanostructure Science and Technology (CINSaT), University of Kassel, Heinrich-Plett-Straße 40, D-34132 Kassel, Germany*
[3]*Department of Materials and Life Sciences, Sophia University, Chiyoda-ku, Tokyo 102-8554, Japan*

The angular correlation functions (ACFs) of a pair of Lyman-α photons in photodissociation of H$_2$ and D$_2$ are measured with linearly polarized incident light at a 33.66-eV incident photon energy in a wider angular range at a narrower angular step with smaller distortion than before [Y. Nakanishi *et al.*, Phys. Rev. A **90**, 043405 (2014)] so that we identify the atom-pair state emitting the pair of Lyman-α photons and find out whether the atom pair is entangled or not. Searching for reasonable 2p atom-pair states that reproduce the experimental ACFs to solve the issue, we show that hydrogen molecules are photoexcited to the $Q_2\,^1\Pi_u(1)$ state in the Franck-Condon region and then the $Q_2\,^1\Pi_u(1)$ state comes to superpose with the $Q_2\,^3\Sigma_u^+(2)$ state as the internuclear distance increases to infinity. The superposition is brought about by the spin-orbit coupling, which is effective around infinite internuclear distance because the potential-energy curves of those states are close to each other, but is negligibly small around the Franck-Condon region because they are apart from each other. The 2p atom pairs turn out to be in the 1_u superposition state, which is entangled. We therefore conclude that an entangled pair of hydrogen atoms is spontaneously produced through the photodissociation of a hydrogen molecule, and the entanglement originates from the 1_u symmetry properties, which are invariant during the dissociation from the Franck-Condon region towards infinite internuclear distance.
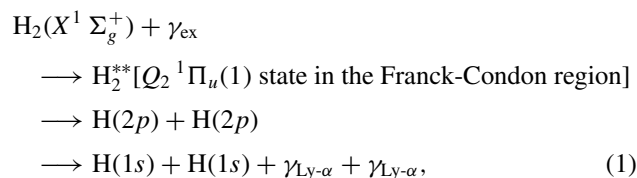
I. INTRODUCTION

Investigations on entanglement in massive quantum particles have been becoming active in atomic and molecular physics as reviewed in Ref. [1] because the entanglement is essential for understanding composite quantum systems. There is a possibility that a breakup of molecules, i.e., molecular dissociation, is a promising source of entangled systems of atoms, which approach is passive and thus remarkable because entangled systems of massive quantum particles are, in general, produced with active control techniques [2,3]. In fact Miyagi *et al.* [4] and Jänkälä *et al.* [5] have theoretically shown the possibility that an entangled pair of H(2p) atoms is produced through photodissociation of a hydrogen molecule. According to their investigations the entanglement originates from the symmetry properties that the electronic state of the 2p atom pair possesses. It is hence a significant subject to reveal the electronic state of the 2p atom pairs in the photodissociation of H$_2$ so that we substantiate the production of the entangled 2p atom pairs without any active control technique, a subject which is achieved with measuring the angular correlation function (ACF) of a pair of Lyman-α photons emitted by 2p atoms [4,5]. In regard to a pair of hydrogen atoms in other states, Robert *et al.* reported that a pair of metastable H(2s) atoms was produced through dissociation of a hydrogen molecule mediated by electron collisions [6]. The same group

has planned to substantiate the production of an entangled pair of H(2s) atoms by means of atomic interferometry [7]. The investigation has just begun on the production of entangled systems of fragment atoms through molecular dissociation. As for the decay processes of an entangled pair of excited atoms, Sancho and Plaja [8] theoretically investigated the radiative decay process of an entangled pair of a He(2^1S) atom and a He(2^3S) atom and predicted that the decay rates of the metastable He atoms in an entangled pair were different from those in a product pair.

Our group [9–11] measured the ACFs of a pair of Lyman-α photons emitted by a pair of H(2p) atoms in the dissociative photoexcitation to the doubly excited $Q_2\,^1\Pi_u(1)$ state of H$_2$ molecules, process (1) below, and compared the experimental ACFs with the theoretical ones to find out whether or not the 2p atom pair is entangled in accordance with the predictions [4,5]:

$$H_2(X^1\Sigma_g^+) + \gamma_{ex}$$
$$\longrightarrow H_2^{**}[Q_2\,^1\Pi_u(1) \text{ state in the Franck-Condon region}]$$
$$\longrightarrow H(2p) + H(2p)$$
$$\longrightarrow H(1s) + H(1s) + \gamma_{Ly-\alpha} + \gamma_{Ly-\alpha}, \qquad (1)$$

where γ_{ex} is a linearly polarized incident photon and $\gamma_{Ly-\alpha}$ a Lyman-α photon. Typical distance between the two H(2p) atoms reaches 93 μm when the H(2p) atoms emit the Lyman-α photons, as calculated from the incident photon energy (33.66 eV as mentioned later), the dissociation limit of H(2p)
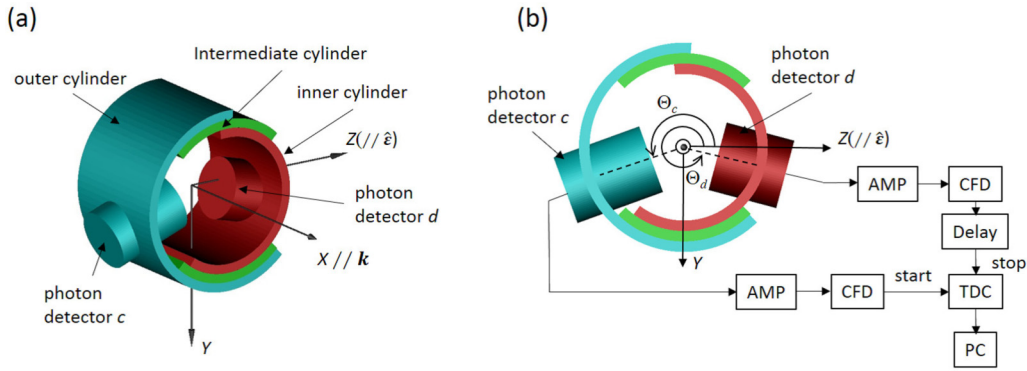
*hosakak@chem.titech.ac.jp

FIG. 1. Experimental setup. The left panel (a) is a schematic view and the right panel (b) shows arrangements of the photon detectors c and d when facing into the propagation direction of the incident light (the photon detectors are placed on the plane perpendicular to the incident light beam). The gas cell consists of three coaxial cylinders, of which symmetry axis coincides with the incident light beam. The incident light with the wave-number vector $\boldsymbol{k}$ travels down the space-fixed X axis and the space-fixed Z axis points to the direction of the unit polarization vector of the linearly polarized incident light denoted by $\hat{\boldsymbol{\varepsilon}}$. The origin of the space-fixed XYZ frame is taken at the crossing point of the three axes, i.e., the axes of the two detectors and the axis of the incident light beam, which crosses the axes of the detectors at right angles. The positive directions of the detector angles Θ_c and Θ_d, which are measured from the unit polarization vector $\hat{\boldsymbol{\varepsilon}}$, are shown in (b). AMP: amplifier; CFD: constant-fraction discriminator; TDC: time-to-digital converter; PC: personal computer.

+ H(2p) (Table II in [12]), and the lifetime of H(2p) atoms, i.e., 1.6 ns (pp. 200–201 in Ref. [13]). The distance between two D(2p) atoms is shortened to approximately $(1/\sqrt{2}) \times 93$ μm if an H_2 molecule is replaced with a D_2 molecule in process (1). The cross sections of the photodissociation (1) were experimentally measured as functions of the incident photon energy [14–16], and it has been well substantiated from the discussion on those cross-section curves that only the $Q_2\,^1\Pi_u(1)$ state is responsible for the production of $2p$ atom pairs in the photoexcitation of H_2 and D_2 in the range of the incident photon energy 30–40 eV [14–16]. Nakanishi *et al.* [11] showed that the experimental ACF was not in agreement with the theoretical ACF [4,5] for the pair of H(2p) atoms in the $Q_2\,^1\Pi_u(1)$ state at infinite internuclear distance.

In the present experiment the ACFs of a pair of Lyman-α photons in the photodissociation of H_2 and D_2 are measured in a wider angular range with a narrower angular step with smaller distortion than before [11]. We aim to identify the atom-pair state in process (1) through a comprehensive search for the $2p$ atom-pair state that is reasonably accessed from the $Q_2\,^1\Pi_u(1)$ state and reproduces the experimental ACFs, and to find out whether or not the $2p$ atom pairs in process (1) are entangled.

II. EXPERIMENTS

A. Experimental setup

The experiments were carried out at the bending beamline BL20A [17] of the Photon Factory, Institute of Materials Structure Science, KEK. The experimental setup was the same as that used in the early experiment for measuring ACFs [11], and is illustrated in Fig. 1.

Linearly polarized light, traveling down the space-fixed X axis, was introduced into a gas cell filled with H_2 or D_2 gas, and the unit polarization vector of the incident light $\hat{\boldsymbol{\varepsilon}}$ is on the space-fixed Z axis. We refer to the space-fixed XYZ frame in detail in Sec. IV A. The polarization degree of the incident light is approximately 0.8 [18,19] and the spot size is 2 mm

$\times$ 2 mm. The incident photon energy was 33.66 eV as in the early experiments [9–11] since this photon energy gives the maximum value of the cross sections for emission of a pair of Lyman-α photons for H_2 [14–16], and the energy width of the incident photons was 140 meV. The flux of incident photons passing through an exit of the gas cell was recorded with measuring the photocurrent of an Au plate. The photon detectors c and d on the plane perpendicular to the incident light beam are rotated over the axis of the incident light beam, i.e., the space-fixed X axis, plane which is referred to as the dipole plane [5]. The rotation angles of the detectors c and d, Θ_c and Θ_d, respectively, are measured from the unit polarization vector of the incident light $\hat{\boldsymbol{\varepsilon}}$, which is parallel to the space-fixed Z axis. The positive directions of the angles Θ_c and Θ_d are shown in Fig. 1(b): the angles $\Theta_{c/d}$ are a part of Euler angles ($\Phi_{c/d} = 3\pi/2$, $\Theta_{c/d}$, $\Psi_{c/d} = 0$). This definition of the rotation angles is the same as in Refs. [4] and [9–11], and slightly different from that in Ref. [5]. The minimum value of $|\Theta_c - \Theta_d|$ is $120°$. The direction of the unit polarization vector of the incident light $\hat{\boldsymbol{\varepsilon}}$ was experimentally determined with the measurement of the angular distribution of photoelectrons from He as mentioned in [11].

B. Coincidence measurements between two Lyman-α photons

Each photon detector consists of a 1-mm-thick MgF_2 window and a microchannel plate coated with CsI, a detector which provides a filter range of approximately 115–200 nm in wavelength. Only Lyman-α photons, with a 121.6-nm wavelength for H atoms, are detected at a 33.66-eV incident photon energy. Molecular fluorescence is unlikely to be emitted by doubly excited hydrogen molecules since fluorescent processes are in general much slower than autoionization and neutral dissociation. The wavelength of the Lyman-β fluorescence, 102.6 nm for H atoms, is out of the detection range. Other fluorescence of atomic hydrogen besides the Lyman series does not lie in the vacuum ultraviolet range. The solid angle subtended by each detector is 0.64 sr as
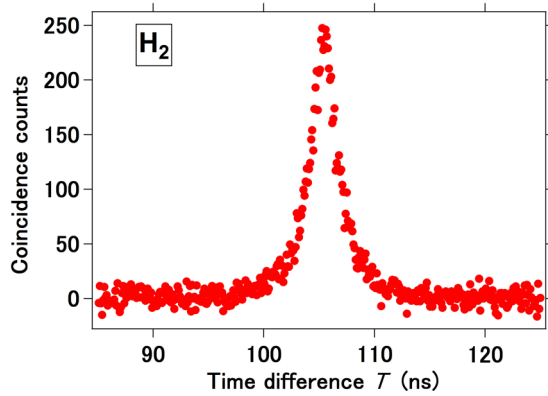
FIG. 2. An example of the two-photon coincidence time spectra. This time spectrum was measured at a 33.66-eV incident photon energy, a 0.4-Pa H_2 gas pressure, and a set of detector angles (Θ_c, Θ_d) = ($-90°$, $90°$). The accidental coincidence counts have been subtracted following the method described in Ref. [11]. The four channels of the time-to-digital converter in Fig. 1(b) are binned to be 0.1004 ns/channel.

in the early experiments [9–11]. The detection time by the detector d, t_d, is measured with respect to the detection time by the detector c, t_c, with a coincidence system shown in Fig. 1(b) and the number of events that the time difference $t_d - t_c$ is equal to T is recorded against T so that a two-photon coincidence time spectrum is obtained. One example recorded at a 0.4-Pa H_2 gas pressure is shown in Fig. 2, where the accidental coincidence counts have been subtracted in the manner described in detail in the early paper [11]. The decay times on both sides are in good agreement with the lifetime of the 2p state, 1.6 ns (pp. 200–201 in Ref. [13]), as expected.

The sample gas pressure should be carefully chosen so that the ACFs are not influenced by secondary processes such as reactions of 2p atoms with hydrogen molecules. Pressure in the gas cell was in fact lower than approximately 1 Pa for H_2 and D_2 gas because it has been confirmed that the angle-resolved two-photon coincidence count rates are proportional to the D_2 gas pressure up to approximately 2 Pa [15], a result indicating that secondary processes do not play a role in the pressure range lower than approximately 2 Pa. The target gas

pressure was kept constant within a variation of less than ±4% during the coincidence measurement at a given set of Θ_c and Θ_d. The false coincidence counts due to cosmic muons, 0.4×10^{-3}–1.2×10^{-3} cps depending on angles, were reported in the same apparatus as that used in the present experiments [11]. In the present range of the target gas pressure, the ratio of the false coincidence counts to the two-photon coincidence counts was less than 1%, and the false counts were not hence subtracted.

C. Measuring the angular correlation functions of a pair of Lyman-α photons

In the present experiment we measure the experimental ACFs for the following arrangements of the detectors c and d: (a) $\Theta_d = \Theta_c + 180°$, (b) $\Theta_d = -\Theta_c$, (c) $\Theta_d = -\Theta_c + 180°$, arrangements which are illustrated in Fig. 3. The arrangement (a) is referred to as the opposite arrangement and those in (b) and (c) are referred to as the nonopposite arrangements.

The ACF of a pair of Lyman-α photons is equivalent to the cross section for emission of a pair of Lyman-α photons differential with respect to solid angles of emitted photons, $\frac{d^2\sigma}{d\Omega_c d\Omega_d}$. Early papers [15,16] show how the two-photon coincidence count rate $\dot{N}_{cd}(\Theta_c, \Theta_d)$ is related to the cross section $\frac{d^2\sigma}{d\Omega_c d\Omega_d}$, the target gas pressure P, and photocurrent from the Au plate i_{Au}:

$$\frac{\dot{N}_{cd}(\Theta_c, \Theta_d)}{P i_{\text{Au}}} = C G_{cd}(\Theta_c, \Theta_d) \eta_{cd} \left\langle \frac{d^2\sigma}{d\Omega_c d\Omega_d} \right\rangle (\Theta_c, \Theta_d),$$

(2)

where $G_{cd}(\Theta_c, \Theta_d)$ is a geometric factor, η_{cd} is a coincidence detection efficiency of the photon detectors for Lyman-α photons, $\langle \frac{d^2\sigma}{d\Omega_c d\Omega_d} \rangle$ is the differential cross section averaged with the present angular resolution, and C is a constant independent of (Θ_c, Θ_d). The geometric factor $G_{cd}(\Theta_c, \Theta_d)$ is an integral of the product of two solid angles subtended by the detectors c and d over the interaction region, and it turned out from ray tracing of the Lyman-α photon that the factor was independent of (Θ_c, Θ_d) [11]. The plot of the values of the left-hand side of Eq. (2) against (Θ_c, Θ_d) hence gives the ACF.
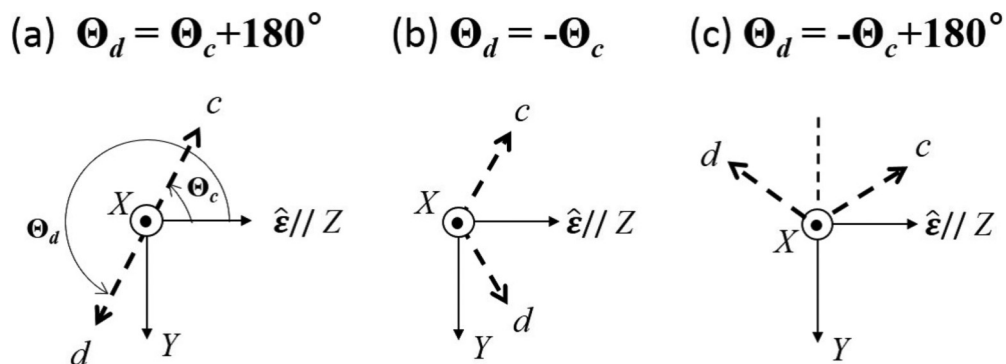

FIG. 3. Arrangements of the photon detectors c and d with respect to the space-fixed XYZ frame, where the Z axis points to the unit polarization vector of the linearly polarized incident light $\hat{\varepsilon}$ and the X axis points to the propagation direction of the incident light. This figure is the view when facing into the propagation direction of the incident light. The positive directions of the angles Θ_c and Θ_d are indicated. The ACFs of a pair of Lyman-α photons for H_2 and D_2 are measured for the arrangements (a)–(c).
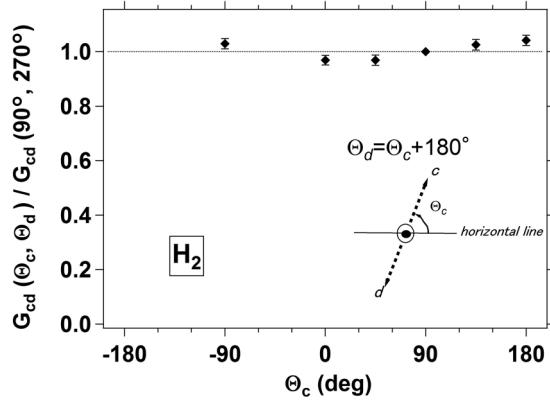
FIG. 4. The angular dependence of the geometric factor $G_{cd}(\Theta_c, \Theta_d)$, which was obtained through measuring the values of the left-hand side of Eq. (3) for the arrangement (a) in Fig. 3 with the circularly polarized incident light at a 33.6-eV incident photon energy and at a 0.4-Pa H_2 gas pressure. The angle Θ_c is measured not from the unit polarization vector of the incident light but from the horizontal direction in contrast to measuring the ACF with the linearly polarized incident light. This result shows the flatness of the angular characteristics in the present apparatus (see the text for details).

In fact, however, we carried out reference measurements at a set of constant angles $(\Theta_c, \Theta_d) = (-90°, 90°)$ to cancel out a possible but small and slow change of $CG_{cd}\eta_{cd}$ in Eq. (2) during the measurement of an ACF, and based on the reference measurements the following relation is obtained:

$$\frac{[\dot{N}_{cd}(\Theta_c, \Theta_d)/(Pi_{\text{Au}})]}{\frac{1}{2}\{[\dot{N}'_{cd}(-90°, 90°)/(P'i'_{\text{Au}})] + [\dot{N}''_{cd}(-90°, 90°)/(P''i''_{\text{Au}})]\}}$$

$$= \left\langle \frac{d^2\sigma}{d\Omega_c d\Omega_d} \right\rangle (\Theta_c, \Theta_d) / \left\langle \frac{d^2\sigma}{d\Omega_c d\Omega_d} \right\rangle (-90°, 90°), \quad (3)$$

where ′ and ″ mean the reference measurements before and after the measurement of $\dot{N}_{cd}(\Theta_c, \Theta_d)$, respectively, and the factor $CG_{cd}\eta_{cd}$ is considered unchanged during the measurements of $\dot{N}'_{cd}$, $\dot{N}_{cd}$, and $\dot{N}''_{cd}$. We eventually plot the values of the left-hand side of Eq. (3) against (Θ_c, Θ_d) to obtain the ACF of a pair of Lyman-α photons.

The values of the left-hand side of Eq. (3) were measured as a function of (Θ_c, Θ_d) for the arrangement (a) in Fig. 3 using circularly polarized incident light to experimentally substantiate that the geometric factor $G_{cd}(\Theta_c, \Theta_d)$ is independent of (Θ_c, Θ_d). Because of physical reasons the ACF, $\frac{d^2\sigma}{d\Omega_c d\Omega_d}$, due to the circularly polarized light is expected to be independent of the direction of the line joining the detectors c and d [see Fig. 3(a)] and the left-hand side of Eq. (3) in this case consequently expresses the angular dependence of the geometric factor. The experiment was carried out at the undulator beam line BL28B [20] of the Photon Factory with a 33.6-eV incident photon energy and 0.4-Pa H_2 gas pressure, and the result, $G_{cd}(\Theta_c, \Theta_d)/G_{cd}(90°, 270°)$ vs Θ_c, is shown in Fig. 4. The distortion from the expected flatness, horizontal dotted line, has turned out to be at most $\pm 4\%$. There remains a possibility that the angular dependence of $G_{cd}(\Theta_c, \Theta_d)$ at the BL20A is different from that at the BL28B shown in Fig. 4 because the spot size of the incident light beam at the

BL28B is much smaller than that at the BL20A, 2 mm × 2 mm. The ACFs measured at the BL28B and BL20A with the linearly polarized incident light, however, are in good agreement with each other [11], and we hence conclude that the geometric factor $G_{cd}(\Theta_c, \Theta_d)$ at the BL20A is as flat as in Fig. 4.

III. RESULTS

In Fig. 5 shown are the experimental ACFs of a pair of Lyman-α photons in the photodissociation of H_2 (○) and D_2 (◇) with the linearly polarized incident light at the photon energy of 33.66 eV. The ACFs for the opposite arrangement [the arrangement (a) in Fig. 3] are shown in the left panel and those for the nonopposite arrangements [the arrangements (b) and (c) in Fig. 3] are shown in the right panel. The experimental ACFs for the two nonopposite arrangements are displayed in the same panel of Fig. 5 because the theoretical ACFs [4,5] for the nonopposite arrangement (b) in Fig. 3 are the same as those for the other nonopposite arrangement (c) in Fig. 3. The error bars were obtained from the uncertainty of each two-photon coincidence count rate in the left-hand side of Eq. (3) using the law of the propagation of errors. The alignment of the apparatus in the present experiment was better than that in the early experiment [11], which was substantiated with the angular distributions of photoelectrons from He and Lyman-α photons from H_2 or D_2, and the ACFs with smaller distribution were obtained as a result. The anisotropy of the experimental ACFs for H_2 and D_2 is so weak that the values at the reference angles of $(\Theta_c, \Theta_d) = (-90°, 90°)$ are approximately set equal to $1/(4\pi)^2$ sr^{-2}: the ACF expresses the probability density for the detection of photon pairs and it is hence normalized to unity when integrated over the entire range of the solid angles for the detectors c and d. The absolute values of the experimental ACFs in Fig. 5 hence have a small uncertainty of a constant multiple, which is in the range 1–1.2. The present ACF for H_2 is consistent with the previous one for H_2 measured at the same incident photon energy in a narrower angular range with a wider angular interval [11]. The ACFs for H_2 and D_2 are almost identical as seen in Fig. 5, while the ratio of the initial population, (the odd number J)/(the even number J), is 3 in H_2 and it is 1/2 in D_2 (J is the quantum number of the total angular momentum of H_2 and D_2 in the ground electronic states) (p. 134 in Ref. [21]). The negligible isotope effect on the ACFs shows that the electronic motion dominates the state of a pair of Lyman-α photons and the nuclear motion gives just a small effect on the state of a photon pair. We identify the electronic state of a pair of the $2p$ atoms produced in process (1) and find out whether the atom pair is entangled or not in the following section.

IV. DISCUSSION

In this section we search for a state of a pair of $2p$ atoms that is reasonably accessed from the precursor $Q_2\,^1\Pi_u(1)$ state in process (1) and gives the ACF in agreement with the
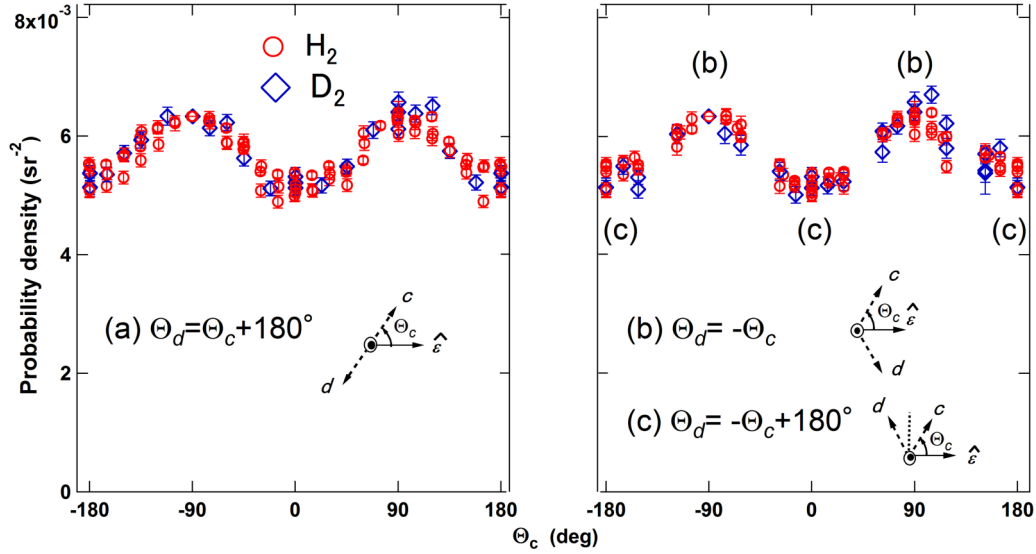
FIG. 5. The experimental ACFs of a pair of Lyman-α photons in the photodissociation of H_2 ($\bigcirc$) and D_2 ($\diamondsuit$) at the incident photon energy of 33.66 eV. The left panel shows the ACFs for the opposite arrangement (a) in Fig. 3, and the right panel shows those for the nonopposite arrangements (b) and (c) in Fig. 3. The error bars were obtained from the uncertainty of each two-photon coincidence count rate in the left-hand side of Eq. (3) using the law of the propagation of errors.

experimental ACFs in Fig. 5, and identify the state as the $2p$ atom-pair state in process (1). We rely on the following framework to solve the issue:

(1) The Born-Oppenheimer approximation is used and only electronic states are considered at infinite internuclear distance.

(2) The nonadiabatic radial coupling between two adiabatic electronic states is taken into account. The nonadiabatic rotational coupling, however, is not taken into account because the potential-energy curves of the doubly excited states of H_2 are repulsive [22–26] and the kinetic energy of the relative motion of the two nuclei, 8.8 eV, at a 33.66-eV incident photon energy, is much higher than the rotational energy, in which situation the axial recoil approximation holds [27]. The internuclear axis does not rotate against the space-fixed frame during the molecular dissociation in process (1) under the axial recoil approximation.

(3) The spin-orbit coupling is neglected.

The doubly excited Q_2 states of H_2 resulting in the $H(n=2) + H(n=2)$ limit were intensively studied [28]: the potential-energy curves were calculated in the range of the internuclear distance from $3a_0$ up to the distance of the asymptotic van der Waals regime and their dissociation limits, i.e., $H(2s) + H(2s)$, $H(2s) + H(2p)$, or $H(2p) + H(2p)$, were identified. In Table I are listed all those doubly excited Q_2 states together with their dissociation limits. It follows that a pair of atoms in any Q_2 state in the first or third group in Table I emits a pair of Lyman-α photons observed in this experiment. We hence calculate the ACFs of a pair of Lyman-α photons originating from the Q_2 states in the first or third group that are reasonably accessed from the precursor $Q_2\,^1\Pi_u(1)$ state in process (1), and compare the calculated ACFs with the experimental ones in Fig. 5. The method for the calculation of the ACF is mentioned in the following subsection.

A. Calculation of angular correlation functions of a Lyman-α photon pair

We calculate the ACF of a pair of Lyman-α photons emitted by an atom pair in a given electronic state along the line mentioned in Ref. [4]. In Fig. 6, the frames of reference, i.e., the space-fixed XYZ frame and molecular xyz frame, are shown. The space-fixed frame is partly mentioned in Sec. II and the comprehensive explanation is given here. The origin of the XYZ frame is taken at a point on the axis of the incident light, which travels down the positive direction of the X axis.

TABLE I. The doubly excited Q_2 states correlating with the $n = 2 + n = 2$ dissociation limit.[a]

States	Dissociation limits
$^1\Sigma_g^+(2),\ ^3\Sigma_u^+(2)\ [1_u]$ [b]	
$^1\Pi_g(2),\ ^3\Pi_u(2)\ [1_u]$	
$^1\Pi_u(1)\ [1_u],^c\quad ^3\Pi_g(1)$	$2p + 2p$
$^1\Sigma_u^-(1),\ ^3\Sigma_g^-(1)$	
$^1\Delta_g(1),\ ^3\Delta_u(1)\ [1_u]$	
$^1\Sigma_g^+(3),\ ^3\Sigma_u^+(3)\ [1_u]$	
$^1\Pi_g(1),\ ^3\Pi_u(1)\ [1_u]$	
$^1\Pi_u(2)\ [1_u],\ ^3\Pi_g(2)$	$2s + 2p$
$^1\Sigma_u^+(1),\ ^3\Sigma_g^+(1)$	
	superposition of
$^1\Sigma_g^+(1),\ ^3\Sigma_u^+(1)\ [1_u]$	$2p + 2p$ and
$^1\Sigma_g^+(4),\ ^3\Sigma_u^+(4)\ [1_u]$	$2s + 2s$

[a]From Ref. [28].
[b]The 1_u states arising from the $n = 2 + n = 2$ limit are shown right to the corresponding L_z eigenstates, being enclosed by angled brackets (see Sec. IV D for details).
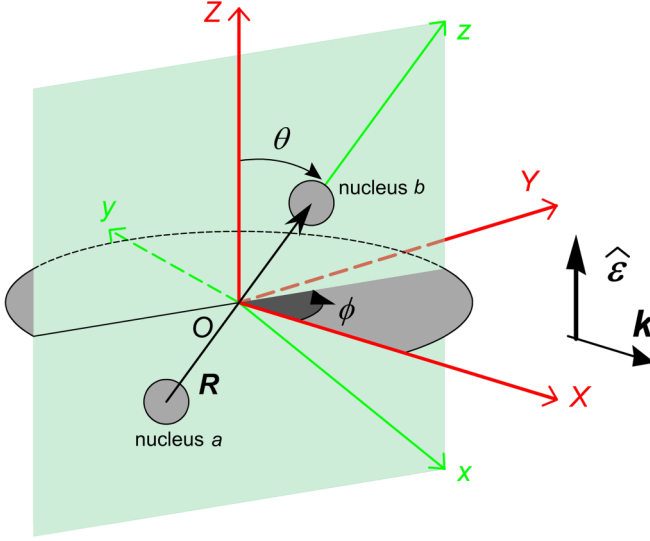[c]The precursor state in process (1).

FIG. 6. The space-fixed frame, the XYZ frame, and the molecular frame, the xyz frame, for calculating the ACF of a pair of Lyman-α photons emitted by a pair of hydrogen atoms. The unit polarization vector of the linearly polarized incident light is denoted by $\hat{\mathbf{\varepsilon}}$ and the wave-number vector of the incident light is denoted by $\mathbf{k}$. Two nuclei are labeled a and b. See Sec. IV A for details.

The Z axis points to the direction of the unit polarization vector of the linearly polarized incident light $\hat{\mathbf{\varepsilon}}$. The Y axis is taken so that the XYZ frame is a right-handed system. The directions of the two photon detectors c and d are specified by the Euler angles $(\Phi_{c/d}, \Theta_{c/d}, \Psi_{c/d} = 0)$ in reference to the space-fixed XYZ frame, provided the detectors are originally on the $+Z$ axis. In the present experiments $\Phi_{c/d}$ are held fixed to $3\pi/2$ as mentioned in Sec. II A.

The electronic states of a hydrogen molecule and a pair of hydrogen atoms are expressed in reference to the molecular xyz frame. The pair of hydrogen atoms is considered a hydrogen molecule with infinite internuclear distance. The two nuclei in the hydrogen molecule are labeled a and b, and the two electrons are labeled 1 and 2. The z axis points from the nucleus a to b. The origin of the xyz frame is taken at the midpoint between the nucleus a and b, and coincides with the origin of the XYZ frame as seen in Fig. 6. The molecular xyz frame, also a right-handed system, is given in reference to the space-fixed XYZ frame with the Euler angles $(\phi, \theta, \chi = 0)$ so that the unit polarization vector of the linearly polarized incident light, $\hat{\mathbf{\varepsilon}}$, is on the xz plane (the light green panel in Fig. 6) and the y axis is on the XY plane (the gray circle in Fig. 6).

We investigate the time evolution of a given state of a $2p$ atom pair to obtain a state of a pair of the Lyman-α photons $|\Gamma\rangle$. The two-photon correlation function $G^{(2)}(\mathbf{r}_c, t_c, \mathbf{r}_d, t_d)$ in quantum optics [29] is then calculated for the photon-pair state $|\Gamma\rangle$ following Ref. [4], function which is proportional to the probability density of detecting a photon pair at the time t_c and t_d by the detector c at the position $\mathbf{r}_c$ and detector d at $\mathbf{r}_d$, respectively. The function $G^{(2)}(\mathbf{r}_c, t_c, \mathbf{r}_d, t_d)$ for the photon-pair state $|\Gamma\rangle$ hence gives the ACF of the pair of Lyman-α photons in $|\Gamma\rangle$. The explicit expression of $G^{(2)}(\mathbf{r}_c, t_c, \mathbf{r}_d, t_d)$

for the photon-pair state $|\Gamma\rangle$ is given below:

$$
\begin{aligned}
&G^{(2)}(\mathbf{r}_c, t_c, \mathbf{r}_d, t_d) \\
&= \langle\Gamma|\, \mathbf{E}^{(-)}(\mathbf{r}_c, t_c)\mathbf{E}^{(-)}(\mathbf{r}_d, t_d)\mathbf{E}^{(+)}(\mathbf{r}_d, t_d)\mathbf{E}^{(+)}(\mathbf{r}_c, t_c)\,|\Gamma\rangle,
\end{aligned}
\tag{4}
$$

where $\mathbf{E}^{(+)}$ and $\mathbf{E}^{(-)}$ are the positive and negative frequency parts of the electric-field operator, respectively, and line up in the normal order. The ACF calculated in this manner involves the Euler angles $(\phi, \theta, \chi = 0)$ that determines the molecular frame in reference to the space-fixed frame, and the ACF is hence averaged with the weight of the distribution of the z-axis direction, i.e., the distribution of the dissociation direction, which is expressed as $[3/(8\pi)]\sin^2\theta$ in process (1) under the axial recoil approximation [27]. This function is obtained from the probability density for the $\Sigma \to \Pi$ excitation with the Euler angles $(\phi, \theta, \chi = 0)$ held fixed [see Eq. (26)] with considering the axial recoil approximation.

B. $Q_2\,{}^1\Pi_u(1)$ state at infinite internuclear distance as a $2p$ atom-pair state

We first calculate the ACF of a pair of Lyman-α photons emitted by an atom pair in the $Q_2\,{}^1\Pi_u(1)$ state at infinite internuclear distance to compare with the experimental ACFs in Fig. 5 since the precursor $Q_2\,{}^1\Pi_u(1)$ state in process (1) adiabatically correlates with the $2p + 2p$ dissociation limit as shown in Table I.

The $Q_2\,{}^1\Pi_u(1)$ state at infinite internuclear distance $|{}^1\Pi_u; \eta, R \to \infty\rangle\, |\chi_{0\,0}^e\rangle$ is written as

$$
\begin{aligned}
&|{}^1\Pi_u; \eta, R \to \infty\rangle\, |\chi_{0\,0}^e\rangle \\
&= (1/\sqrt{2})\big(|{}^1\Pi_u^{L_z=+1}; R \to \infty\rangle \\
&\quad + e^{i\eta}|{}^1\Pi_u^{L_z=-1}; R \to \infty\rangle\big) \otimes |\chi_{0\,0}^e\rangle,
\end{aligned}
\tag{5}
$$

$$
|\chi_{0\,0}^e\rangle = (1/\sqrt{2})[|\alpha(1)\rangle\, |\beta(2)\rangle - |\beta(1)\rangle\, |\alpha(2)\rangle],
\tag{6}
$$

where the phase η ranges from 0 to 2π and R is the internuclear distance. The ket vectors $|\alpha\rangle$ and $|\beta\rangle$ are spin eigenstates of an electron. A Π level has twofold degeneracy: one component has the quantum number $L_z = 1$ and the other has $L_z = -1$, where the quantum number L_z expresses projection of the electron orbital-angular momentum on the z axis, the axis joining the nucleus a and b, in the unit of $\hbar$. The $L_z = 1$ component of the ${}^1\Pi_u$ level is written as a ket vector $|{}^1\Pi_u^{L_z=+1}\rangle$ and the $L_z = -1$ component as $|{}^1\Pi_u^{L_z=-1}\rangle$ in Eq. (5). The explicit forms of the ket vectors $|{}^1\Pi_u^{L_z=\pm1}; R \to \infty\rangle$ are given in Ref. [4] and rewritten below:

$$
\begin{aligned}
&|{}^1\Pi_u^{L_z=\pm1}; R \to \infty\rangle \\
&= (1/2)\big[\,|2p_{\pm1}^a(1)\rangle\, |2p_0^b(2)\rangle + |2p_{\pm1}^a(2)\rangle\, |2p_0^b(1)\rangle \\
&\quad - |2p_0^a(1)\rangle\, |2p_{\pm1}^b(2)\rangle - |2p_0^a(2)\rangle\, |2p_{\pm1}^b(1)\rangle\,\big],
\end{aligned}
\tag{7}
$$

where a ket vector $|2p_m^a(1)\rangle$ $(m = -1, 0, 1)$, for example, means that the electron 1 is bound by the nucleus a and the projection of the electron orbital-angular momentum on the z axis is m in the unit of $\hbar$. A ket vector $|2p_m^a(i)\rangle$ $(i = 1, 2)$ is given through the translation of a ket vector

$|2p_m(i)\rangle$ along the z axis by $-(1/2)\boldsymbol{R}$, where $\boldsymbol{R}$ denotes the relative position vector of the two nuclei in reference to the nucleus a (see Fig. 6). A ket vector $|2p_m^b(i)\rangle$ ($i = 1, 2$) is given through the translation of a ket vector $|2p_m(i)\rangle$ along the z axis by $(1/2)\boldsymbol{R}$. We note that $\sigma_{xz}|^1\Pi_u^{L_z=\pm 1}\rangle = -|^1\Pi_u^{L_z=\mp 1}\rangle$ and $\sigma_{xz}|2p_m(i)\rangle = (-1)^m|2p_{-m}(i)\rangle$ ($i = 1, 2$), where σ_{xz} is a reflection operator at the xz plane for electronic states. The electronic states $|^1\Pi_u; \eta, R \to \infty\rangle|\chi_{0\,0}^e\rangle$ and $|^1\Pi_u; \eta + \pi, R \to \infty\rangle|\chi_{0\,0}^e\rangle$ compose a set of eigenstates for the permutation operator of the two identical nuclei a and b. The atom-pair state $|^1\Pi_u; \eta, R \to \infty\rangle|\chi_{0\,0}^e\rangle$ in Eqs. (5)–(7) is entangled because the state of the electron 1 is not definite and the state of the electron 2 is not definite as well, e.g., the projection of the orbital-angular momentum of the electron 1 on the z axis is not definite and that of the electron 2 is not definite as well. The entanglement originates from the symmetry properties that the atom-pair state $|^1\Pi_u; \eta, R \to \infty\rangle|\chi_{0\,0}^e\rangle$ possesses.

The time evolution of the $2p$ atom pairs in the $|^1\Pi_u; \eta, R \to \infty\rangle|\chi_{0\,0}^e\rangle$ state is investigated based on the time evolution of $2p$ atoms shown below ($i = 1, 2$) [4]:

$$|2p_{+1}^a(i)\rangle|\text{vac}\rangle \xrightarrow{\text{time } t \to \infty} |1s^a(i)\rangle|\gamma_a\rangle, \tag{8}$$

$$|2p_{+1}^b(i)\rangle|\text{vac}\rangle \longrightarrow |1s^b(i)\rangle|\gamma_b\rangle, \tag{9}$$

$$|2p_0^a(i)\rangle|\text{vac}\rangle \longrightarrow |1s^a(i)\rangle|\phi_a\rangle, \tag{10}$$

$$|2p_0^b(i)\rangle|\text{vac}\rangle \longrightarrow |1s^b(i)\rangle|\phi_b\rangle, \tag{11}$$

$$|2p_{-1}^a(i)\rangle|\text{vac}\rangle \longrightarrow |1s^a(i)\rangle|\rho_a\rangle, \tag{12}$$

$$|2p_{-1}^b(i)\rangle|\text{vac}\rangle \longrightarrow |1s^b(i)\rangle|\rho_b\rangle, \tag{13}$$

where $|\text{vac}\rangle$ is the vacuum state of the photon field. The ket vectors $|1s^a(i)\rangle$ and $|1s^b(i)\rangle$ are the $1s$ states of a hydrogen atom, where the electron i ($i = 1, 2$) is bound by the nucleus a and b, respectively. The ket vectors $|\gamma\rangle$, $|\phi\rangle$, and $|\rho\rangle$ are states of a single photon emitted by a hydrogen atom through the $2p \to 1s$ transitions of $\Delta m = -1, 0, 1$, respectively. For example, $|\gamma_a\rangle$ is a state of a Lyman-α photon emitted by a

hydrogen atom through the transition $|2p_{+1}^a(1)\rangle \to |1s^a(1)\rangle$ or $|2p_{+1}^a(2)\rangle \to |1s^a(2)\rangle$. It is a good approximation that the spin-orbit coupling is neglected in the radiative transition in a hydrogen atom and the spin eigenstates of electrons consequently remain unaltered. It is found from Eqs. (5)–(7) and (8)–(13) that the $|^1\Pi_u; \eta, R \to \infty\rangle|\chi_{0\,0}^e\rangle|\text{vac}\rangle$ state is evolved in time as follows:

$$
\begin{aligned}
&|^1\Pi_u; \eta, R \to \infty\rangle|\chi_{0\,0}^e\rangle|\text{vac}\rangle \\
&\xrightarrow{t \to \infty} (1/2)[(|\gamma_a\rangle|\phi_b\rangle - |\phi_a\rangle|\gamma_b\rangle) \\
&\quad + e^{i\eta}(|\rho_a\rangle|\phi_b\rangle - |\phi_a\rangle|\rho_b\rangle)] \\
&\quad \otimes (1/\sqrt{2})[|1s^a(1)\rangle|1s^b(2)\rangle + |1s^a(2)\rangle|1s^b(1)\rangle]|\chi_{0\,0}^e\rangle.
\end{aligned}
\tag{14}
$$

Equation (14) is rewritten in a simpler form as shown below:

$$
\begin{aligned}
&|^1\Pi_u; \eta, R \to \infty\rangle|\chi_{0\,0}^e\rangle|\text{vac}\rangle \\
&\xrightarrow{t \to \infty} |\Gamma;\,^1\Pi_u, \eta\rangle|X^1\Sigma_g^+; R \to \infty\rangle|\chi_{0\,0}^e\rangle,
\end{aligned}
\tag{15}
$$

where the photon-pair state $|\Gamma;\,^1\Pi_u, \eta\rangle$ is

$$
\begin{aligned}
|\Gamma;\,^1\Pi_u, \eta\rangle = (1/2)[&(|\gamma_a\rangle|\phi_b\rangle - |\phi_a\rangle|\gamma_b\rangle) \\
&+ e^{i\eta}(|\rho_a\rangle|\phi_b\rangle - |\phi_a\rangle|\rho_b\rangle)],
\end{aligned}
\tag{16}
$$

and the spatial part of the final atom-pair state $|X^1\Sigma_g^+; R \to \infty\rangle$ is

$$
\begin{aligned}
|X^1\Sigma_g^+; R \to \infty\rangle = (1/\sqrt{2})[&|1s^a(1)\rangle|1s^b(2)\rangle \\
&+ |1s^a(2)\rangle|1s^b(1)\rangle].
\end{aligned}
\tag{17}
$$

We thereby obtain the photon-pair state $|\Gamma;\,^1\Pi_u, \eta\rangle$ emitted by the atom pairs in the $|^1\Pi_u; \eta, R \to \infty\rangle|\chi_{0\,0}^e\rangle$ state in Eq. (5) and calculate the two-photon correlation function for the photon-pair state $|\Gamma;\,^1\Pi_u, \eta\rangle$ to obtain the ACF of a pair of Lyman-α photons emitted by the $2p$ atom pairs in the $|^1\Pi_u; \eta, R \to \infty\rangle|\chi_{0\,0}^e\rangle$ state. In Ref. [4], they calculated only the ACF for the $|^1\Pi_u; \pi, R \to \infty\rangle|\chi_{0\,0}^e\rangle$ state. The calculated ACF for the $2p$ atom-pair state $|^1\Pi_u; \eta, R \to \infty\rangle|\chi_{0\,0}^e\rangle$ ($0 \leqslant \eta \leqslant 2\pi$) is averaged with the distribution of the dissociation direction, $[3/(8\pi)]\sin^2\theta$ [see Eq. (26)], and the resulting ACF, $F(\Theta_c, \Phi_c, \Theta_d, \Phi_d;\,^1\Pi_u, \eta)$, has the form of

$$F(\Theta_c, \Phi_c, \Theta_d, \Phi_d;\,^1\Pi_u, \eta) = f(\Theta_c, \Phi_c, \Theta_d, \Phi_d) + (2\cos\eta)g(\Theta_c, \Phi_c, \Theta_d, \Phi_d), \tag{18}$$

$$
\begin{aligned}
f(\Theta_c, \Phi_c, \Theta_d, \Phi_d) = \frac{9}{143\,360\pi^2}\{&1008 - 56[\cos 2(\Theta_c - \Theta_d) + \cos 2(\Theta_c + \Theta_d)] \\
&- 84\cos(\Phi_c - \Phi_d)[\cos 2(\Theta_c - \Theta_d) - \cos 2(\Theta_c + \Theta_d)] \\
&- 28\cos 2(\Phi_c - \Phi_d)[2 - 2\cos 2\Theta_c - 2\cos 2\Theta_d + \cos 2(\Theta_c - \Theta_d) + \cos 2(\Theta_c + \Theta_d)]\},
\end{aligned}
\tag{19}
$$

$$
\begin{aligned}
g(\Theta_c, \Phi_c, \Theta_d, \Phi_d) = \frac{9}{143360\pi^2}\{&84 + 140(\cos 2\Theta_c + \cos 2\Theta_d) + 42[\cos 2(\Theta_c - \Theta_d) + \cos 2(\Theta_c + \Theta_d)] \\
&+ 28\cos(\Phi_c - \Phi_d)[\cos 2(\Theta_c - \Theta_d) - \cos 2(\Theta_c + \Theta_d)] \\
&- 14\cos 2(\Phi_c - \Phi_d)[2 - 2\cos 2\Theta_c - 2\cos 2\Theta_d + \cos 2(\Theta_c - \Theta_d) + \cos 2(\Theta_c + \Theta_d)]\}.
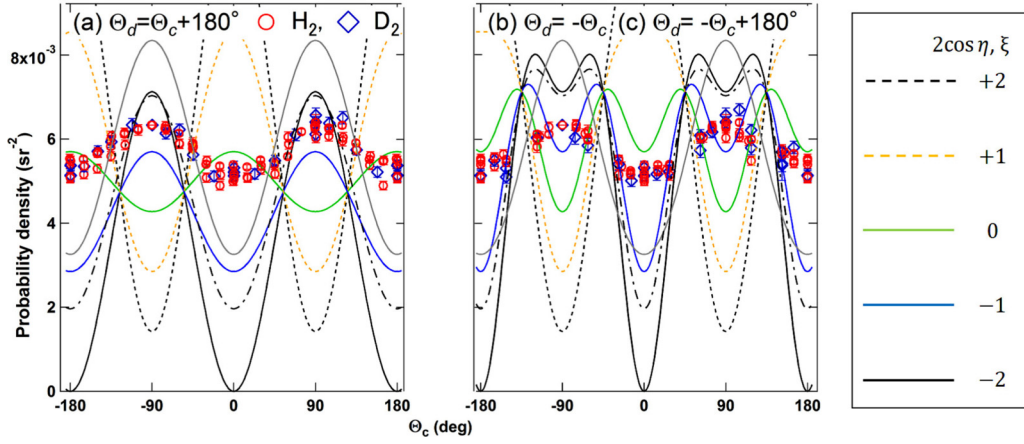\end{aligned}
\tag{20}
$$

FIG. 7. Comparison between the experimental ACFs for H$_2$ ($\bigcirc$) and D$_2$ ($\lozenge$) in Fig. 5 and those calculated for the 2p atom pairs in the Q_2 $^1\Pi_u(1)$ state at infinite internuclear distance (lines). The left panel shows the experimental and theoretical ACFs for the opposite arrangement (a) in Fig. 3, and the right panel shows those for the nonopposite arrangements (b) and (c) because the theoretical ACFs for the arrangement (b) are the same as those for the arrangement (c). The relation between the calculated ACFs [Eq. (18) or (24)] and the values of $2\cos\eta$ or ξ is indicated in the figure, for example, the ACF calculated for $2\cos\eta = -2$ or $\xi = -2$ is drawn with the black solid line. The ACF drawn with the black solid line has been convoluted with the present angular resolution and the convoluted ACF is shown with the black dot-dashed line. Shown with the gray solid line is the ACF calculated by Jänkälä *et al.* [5] for the 2p atom pairs in the Q_2 $^1\Pi_u(1)$ state at infinite internuclear distance.

The ACF in Eq. (18) has been normalized to unity as follows:

$$\int F(\Theta_c, \Phi_c, \Theta_d, \Phi_d; \, ^1\Pi_u, \eta)d\Omega_c d\Omega_d = 1. \quad (21)$$

Shown in Fig. 7 are the ACFs, $F(\Theta_c, \Phi_c, \Theta_d, \Phi_d; \, ^1\Pi_u, \eta)$, for some values of η together with the experimental ACFs for H$_2$ ($\bigcirc$) and D$_2$ ($\lozenge$). The left panel in the figure shows the experimental and theoretical ACFs for the opposite arrangement (a) in Fig. 3, and the right panel shows those for the nonopposite arrangements (b) and (c) because the theoretical ACFs, $F(\Theta_c, \Phi_c, \Theta_d, \Phi_d; \, ^1\Pi_u, \eta)$, for the arrangement (b) are the same as those for the arrangement (c). The calculated ACF for $\eta = \pi$ ($2\cos\eta = -2$), black solid line, has been convoluted with the angular resolution in the present experiment and the convoluted ACF is also shown in Fig. 7, black dot-dashed line, so that we may see the effect of the angular resolution on the calculated ACFs for other values of η. It is obvious that no theoretical ACF for the 2p atom-pair state $|^1\Pi_u; \eta, R \rightarrow \infty\rangle \, |\chi_{0\,0}^e\rangle$ is in agreement with the experimental ACFs of H$_2$ ($\bigcirc$) and D$_2$ ($\lozenge$) even if we consider the uncertainty of the constant multiple in the absolute values of the experimental ACFs mentioned in Sec. III and the effect of the angular resolution.

In the above discussion only the pure ensemble of the atom pairs in the Q_2 $^1\Pi_u(1)$ state is considered. The ensemble of the atom pairs, however, is likely to be the mixed ensemble expressed by the following density operator:

$$\rho_a[^1\Pi_u; \omega(\eta)]$$
$$= \int_{\eta=0}^{\eta=2\pi} d\eta \omega(\eta)$$
$$\times |^1\Pi_u; \eta, R \rightarrow \infty\rangle \, |\chi_{0\,0}^e\rangle \langle \chi_{0\,0}^e| \, \langle^1\Pi_u; \eta, R \rightarrow \infty|, \quad (22)$$

where $\omega(\eta)$ expresses the population function to the $|^1\Pi_u; \eta, R \rightarrow \infty\rangle \, |\chi_{0\,0}^e\rangle$ state with the molecular frame held

fixed in reference to the space-fixed frame, i.e., with the Euler angles (ϕ, θ, $\chi = 0$) held fixed, and is calculated later. The population function $\omega(\eta)$ satisfies the following relation:

$$\int_{\eta=0}^{\eta=2\pi} \omega(\eta)d\eta = 1. \quad (23)$$

The ACF calculated for the photon pairs in the $|\Gamma; \, ^1\Pi_u, \eta\rangle$ state in Eq. (16) is averaged with the population function $\omega(\eta)$ according to Eq. (22) and then the resulting ACF is further averaged with the distribution of the dissociation direction, $[3/(8\pi)]\sin^2\theta$ [see Eq. (26)]. The ACF obtained in this way for the density operator of the atom pairs $\rho_a[^1\Pi_u; \omega(\eta)]$ in Eq. (22) has the form of

$$F(\Theta_c, \Phi_c, \Theta_d, \Phi_d; \, ^1\Pi_u)$$
$$= f(\Theta_c, \Phi_c, \Theta_d, \Phi_d) + \xi g(\Theta_c, \Phi_c, \Theta_d, \Phi_d), \quad (24)$$

$$\xi = \int_{\eta=0}^{\eta=2\pi} 2\omega(\eta) \cos\eta \, d\eta. \quad (25)$$

The value of ξ depends on the population function $\omega(\eta)$, and it is readily seen that $-2 \leqslant \xi \leqslant 2$, whose range is the same as that of $2\cos\eta$ in Eq. (18). The ACF in Eq. (24) is thus equivalent to Eq. (18) and it is hence sufficient to simply show the ACFs given by Eq. (18) in Fig. 7 considering $2\cos\eta$ as ξ.

The population function $\omega(\eta)$ to the $|^1\Pi_u; \eta, R \rightarrow \infty\rangle \, |\chi_{0\,0}^e\rangle$ state at given Euler angles (ϕ, θ, $\chi = 0$), which determine the molecular frame against the space-fixed frame, is obtained through calculating the probability density for the excitation from the $|X^1\Sigma_g^+; R\rangle \, |\chi_{0\,0}^e\rangle$ state to the $|^1\Pi_u; \eta, R\rangle \, |\chi_{0\,0}^e\rangle$ state at the Euler angles (ϕ, θ, $\chi = 0$) and at the equilibrium internuclear distance in the $X^1\Sigma_g^+$ state of H$_2$ and D$_2$. The excitation probability density has been calculated to be

$$(1/\pi)\sin^2(\eta/2)[3/(8\pi)]\sin^2\theta, \quad (26)$$

and $\omega(\eta)$ is hence obtained as

$$\omega(\eta) = (1/\pi)\sin^2(\eta/2). \qquad (27)$$

The distribution of the dissociation direction for Π states $[3/(8\pi)]\sin^2\theta$ mentioned in the present subsection and Sec. IV A is derived from the excitation probability density in Eq. (26) considering the axial recoil approximation. Substituting Eq. (27) into Eq. (25) we obtain $\xi = -1$. The ACF for $\xi = -1$ (the blue solid line in Fig. 7) is not in agreement with the experimental ACFs, and the calculated ACFs for other values of ξ are also not in agreement with the experimental ones. It hence turns out from Fig. 7 that any atom-pair ensemble expressed by $\rho_a[^1\Pi_u; \omega(\eta)]$ in Eq. (22) does not reproduce the experimental ACFs for H_2 and D_2.

Jänkälä *et al.* [5] calculated the angle-differential cross section for the emission of a pair of fluorescence photons in photodissociation of a diatomic molecule, which gives the ACF of a pair of fluorescence photons. They calculated the three transition dipole moments for the absorption of a linearly polarized incident photon, the emission of the first fluorescence photon by a pair of fragment atoms, and the emission of the second fluorescence photon. The products of the three dipole moments were summed over the possible excitation and emission pathways. The absolute square of the summation gives the angle-differential cross section. They applied their method to the calculation of the ACF of a pair of Lyman-α photons in process (1), and the ACF is shown in Fig. 7 with the gray solid line, which again dose not reproduce the experimental ACFs for H_2 and D_2 if their ACF is convoluted with the present angular resolution [11].

In the end we conclude that the $2p$ atom pairs in process (1) are not in the $Q_2 \, ^1\Pi_u(1)$ state at infinite internuclear distance, while the $H_2^{**}(D_2^{**})$ molecules in process (1) are in the $Q_2 \, ^1\Pi_u(1)$ state around the Franck-Condon region as mentioned in Sec. I.

C. Role of the nonadiabatic coupling

The conclusion in the preceding subsection suggests that the inclusion of the nonadiabatic couplings between the precursor $Q_2 \, ^1\Pi_u(1)$ state in process (1) and any state in Table I may lead to discovering the calculated ACF in agreement with the experimental ACFs in Fig. 5. As for nonadiabatic transitions from the $Q_2 \, ^1\Pi_u(1)$ state to any state in Table I, only the nonadiabatic transition to the $Q_2 \, ^1\Pi_u(2)$ state occurs under the framework mentioned at the beginning of Sec. IV. The nonadiabatic transition to the $Q_2 \, ^1\Sigma_u^-(1)$ state from the $Q_2 \, ^1\Pi_u(1)$ state, for example, is unlikely to occur because the transition is brought about by the rotational coupling neglected in the present framework and the potential-energy curve of the $Q_2 \, ^1\Pi_u(1)$ state does not cross that of the $Q_2 \, ^1\Sigma_u^-(1)$ state [24,25]. The consideration of the nonadiabatic transition from the $Q_2 \, ^1\Pi_u(1)$ state to the $Q_2 \, ^1\Pi_u(2)$ state, a transition which was found to occur at $\sim 5.6a_0$ through the radial coupling [15,16,30], does not change the calculated ACFs in Fig. 7 because the $Q_2 \, ^1\Pi_u(2)$ state correlates with the $2s + 2p$ dissociation limit as shown in Table I. The inclusion of the nonadiabatic transition does not lead to the identification of the $2p$ atom-pair states in process (1).

We then discuss the superposition of the $Q_2 \, ^1\Pi_u(1)$ state and $Q_2 \, ^1\Pi_u(2)$ state as in the singly excited states of H_2 [31–33]. The superposition state, if any, emits the pair of the Lyman-α photons in the $|\Gamma; \, ^1\Pi_u, \eta\rangle$ state in Eq. (16) and does not hence reproduce the experimental ACFs in Fig. 5. The superpositions of the $Q_2 \, ^1\Pi_u(1)$ state with other singlet-ungerade states in Table I, the $Q_2 \, ^1\Sigma_u^-(1)$ state and $Q_2 \, ^1\Sigma_u^+(1)$ state, are unlikely to occur under the present framework where the nonadiabatic rotational coupling is neglected. In conclusion of this subsection the inclusion of the nonadiabatic couplings does not lead to the identification of the $2p$ atom-pair states in process (1).

D. Superposition of the $Q_2 \, ^1\Pi_u(1)$ state with a triplet state due to the spin-orbit coupling

We reconsider item (3) in the framework mentioned at the beginning of Sec. IV based on the discussion in Secs. IV B and IV C. It is a good approximation to neglect the spin-orbit coupling around the Franck-Condon region for H_2 and D_2 because the matrix elements of the coupling are smaller than $1 \text{ cm}^{-1} = 0.124$ meV, as seen on p. 245 of Ref. [13] and in Ref. [34], and the difference between the potential-energy curves is, in general, in the order of eV. The transition between a singlet state and a triplet state in Table I is unlikely around the Franck-Condon region as a result. The situation is, however, much different at infinite internuclear distance as seen below. All the potential-energy curves of the 22 states in Table I are degenerate at infinite internuclear distance, and it hence becomes not a good approximation to neglect the spin-orbit coupling there even for H_2 and D_2. We consequently use the revised framework where the items (1) and (2) remain unaltered but the item (3) is replaced with the item $(3)'$ below:

$(3)'$ The spin-orbit coupling is taken into account at infinite internuclear distance while it still remains neglected around the Franck-Condon region.

The precursor $Q_2 \, ^1\Pi_u(1)$ state in process (1) is a L_z eigenstate and is simultaneously a 1_u state as a J_z eigenstate, where J_z is the projection of the electron total-angular momentum on the z axis in the unit of $\hbar$. There are nine 1_u states arising from the $n = 2 + n = 2$ limit in total based on the building-up principle mentioned on pp. 315–322 in Ref. [21]. In Table I, the 1_u states resulting from separate L_z eigenstates are shown right to the corresponding L_z eigenstates, being enclosed by angled brackets. Those 1_u states in Table I are eigenstates of $\hat{H}^{\text{ele}}$ around the Franck-Condon region to a good approximation, where $\hat{H}^{\text{ele}}$ is the electronic Hamiltonian of H_2 or D_2 including the spin-orbit coupling $\hat{H}^{\text{SO}}$, since $\hat{H}^{\text{SO}}$ is neglected around the Franck-Condon region as mentioned above. They are not, however, eigenstates of $\hat{H}^{\text{ele}}$ at infinite internuclear distance as they are since, as mentioned, it becomes not a good approximation to neglect the spin-orbit coupling there. The proper 1_u states at infinite internuclear distance are expressed as the superpositions of the nine 1_u states in Table I, and the nine-state problem has to be solved to obtain the nine superpositions, a problem which is difficult to solve. We hence solve a two-state problem as an approximation of the nine-state problem as mentioned below.
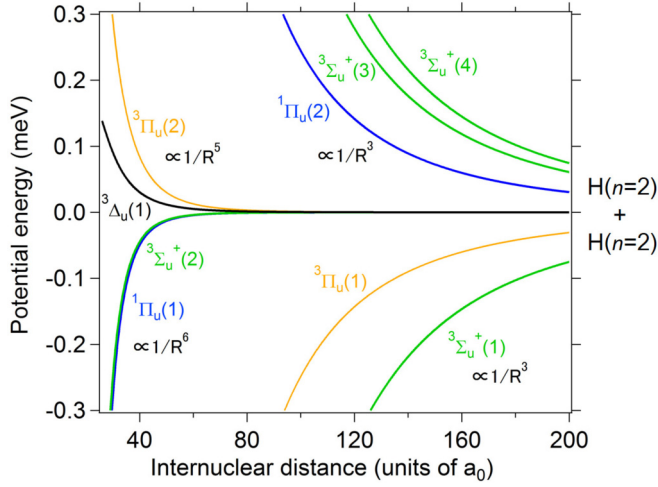
FIG. 8. Potential-energy curves of the $Q_2\,^3\Sigma_u^+(2)$, $Q_2\,^3\Pi_u(2)$, $Q_2\,^1\Pi_u(1)$, $Q_2\,^3\Delta_u(1)$, $Q_2\,^3\Sigma_u^+(3)$, $Q_2\,^3\Pi_u(1)$, $Q_2\,^1\Pi_u(2)$, $Q_2\,^3\Sigma_u^+(1)$, and $Q_2\,^3\Sigma_u^+(4)$ states of H_2 in Table I in the van der Waals regime [28], with each state having one 1_u component. The spin-orbit coupling was not considered in the calculation. Green curves: $^3\Sigma_u^+$ states; orange curves: $^3\Pi_u$ states; blue curves: $^1\Pi_u$ states; black curves: $^3\Delta_u$ states. The leading terms in the $^1\Pi_u(1)$ and $^3\Sigma_u^+(2)$ states are proportional to $1/R^6$, those in the $^3\Pi_u(2)$ and $^3\Delta_u(1)$ states are proportional to $1/R^5$, and those in other states are proportional to $1/R^3$ as shown in the figure, where R is internuclear distance.

In Fig. 8 are shown the potential-energy curves of the nine L_z eigenstates having the 1_u components in Table I in the van der Waals regime without considering the spin-orbit coupling [28]. We seek a 1_u state whose potential-energy curve is much closer to that of the $Q_2\,^1\Pi_u(1)$ state among the nine L_z eigenstates because it is expected from the context of the perturbation theory that states far away from the $Q_2\,^1\Pi_u(1)$ state are not superposed with the $Q_2\,^1\Pi_u(1)$ state quite as much. It is clearly seen that only the $Q_2\,^3\Sigma_u^+(2)$ state is such a state. It hence seems to be a good approximation to solve the two-state problem between the $Q_2\,^1\Pi_u(1)$ $[1_u]$ state and the $Q_2\,^3\Sigma_u^+(2)$ $[1_u]$ state instead of solving the nine-state problem (those 1_u states satisfy the selection rules for matrix elements of $\hat{H}^{SO}$ [35]). In fact we solve the two-state problems between the $J_z = \pm 1$ component of the $Q_2\,^1\Pi_u(1)$ state and the $J_z = \pm 1$ component of the $Q_2\,^3\Sigma_u^+(2)$ state (double-sign corresponds). The low-energy solution is taken in each two-state problem because the $Q_2\,^1\Pi_u(1)$ curve is lower than the $Q_2\,^3\Sigma_u^+(2)$ curve as seen in Fig. 8. In solving the two-state problem, a strong-coupling approximation is used for simplicity, in which approximation the magnitude of the difference of the diagonal matrix elements in the 2×2 matrix of $\hat{H}^{ele}$ is neglected against the magnitude of the off-diagonal matrix elements. We then take a pair of superpositions of the low-energy solution with $J_z = 1$ and that with $J_z = -1$ with the relative phase η $(0 \leqslant \eta \leqslant 2\pi)$ to obtain a pair of 1_u states; one is symmetric and the other is antisymmetric with respect to the permutation operator of the two identical nuclei a and b:

$$|1_u; \eta, \eta_{SO}, R \to \infty\rangle = (1/\sqrt{2})\,|^3\Sigma_u^+; R \to \infty\rangle \left[(1/\sqrt{2})\big(|\chi_{1\,1}^e\rangle - e^{i\eta}\,|\chi_{1\,-1}^e\rangle\big)\right] - (1/\sqrt{2})e^{-i\eta_{SO}}\,|^1\Pi_u; \eta, R \to \infty\rangle\,|\chi_{0\,0}^e\rangle, \quad (28)$$

$$|^3\Sigma_u^+; R \to \infty\rangle = (1/\sqrt{6})\big\{ - \big[\,|2p_0^a(1)\rangle\,|2p_0^b(2)\rangle - |2p_0^a(2)\rangle\,|2p_0^b(1)\rangle\,\big] + \big[\,|2p_{+1}^a(1)\rangle\,|2p_{-1}^b(2)\rangle - |2p_{+1}^a(2)\rangle\,|2p_{-1}^b(1)\rangle$$
$$+\,|2p_{-1}^a(1)\rangle\,|2p_{+1}^b(2)\rangle - |2p_{-1}^a(2)\rangle\,|2p_{+1}^b(1)\rangle\,\big]\big\}, \quad (29)$$

$$\big|\chi_{1\,1}^e\big\rangle = |\alpha(1)\rangle\,|\alpha(2)\rangle, \quad (30)$$

$$\big|\chi_{1\,-1}^e\big\rangle = |\beta(1)\rangle\,|\beta(2)\rangle, \quad (31)$$

where η_{SO} $(0 \leqslant \eta_{SO} \leqslant 2\pi)$ is the phase of the matrix element,

$$\langle^3\Sigma_u^+; R \to \infty|\,\big\langle\chi_{1\,1}^e\big|\,\hat{H}^{SO}(R \to \infty)\,\big|^1\Pi_u^{L_z=+1}; R \to \infty\big\rangle\,\big|\chi_{0\,0}^e\big\rangle, \quad (32)$$

and the $|^1\Pi_u; \eta, R \to \infty\rangle\,|\chi_{0\,0}^e\rangle$ state is given in Eqs. (5)–(7). We also use the result of Ref. [28] in addition to our calculation to obtain the expression of the $|^3\Sigma_u^+; R \to \infty\rangle$ state in Eq. (29). The $|1_u; \eta, \eta_{SO}, R \to \infty\rangle$ and $|1_u; \eta + \pi, \eta_{SO}, R \to \infty\rangle$ states compose a set of eigenstates for the permutation operator of the two identical nuclei a and b, and it is hence sufficient to simply calculate the ACF for the atom pairs in the $|1_u; \eta, \eta_{SO}, R \to \infty\rangle$ state in Eq. (28) $(0 \leqslant \eta \leqslant 2\pi)$.

It is found from Eqs. (28)–(31) and Eqs. (8)–(13) that the $|1_u; \eta, \eta_{SO}, R \to \infty\rangle\,|vac\rangle$ state is evolved in time as follows:

$$|1_u; \eta, \eta_{SO}, R \to \infty\rangle\,|vac\rangle \xrightarrow{t \to \infty} |\Phi; \eta, \eta_{SO}\rangle = (1/\sqrt{2})\,|\Gamma;\,^3\Sigma_u^+\rangle\,|b^3\Sigma_u^+; R \to \infty\rangle \left[(1/\sqrt{2})\big(|\chi_{1\,1}^e\rangle - e^{i\eta}\,|\chi_{1\,-1}^e\rangle\big)\right]$$
$$- (1/\sqrt{2})e^{-i\eta_{SO}}\,|\Gamma;\,^1\Pi_u, \eta\rangle\,|X^1\Sigma_g^+; R \to \infty\rangle\,\big|\chi_{0\,0}^e\big\rangle, \quad (33)$$

where the photon-pair state $|\Gamma;\,^3\Sigma_u^+\rangle$ is

$$|\Gamma;\,^3\Sigma_u^+\rangle = (1/\sqrt{3})(-\,|\phi_a\rangle\,|\phi_b\rangle + |\gamma_a\rangle\,|\rho_b\rangle + |\rho_a\rangle\,|\gamma_b\rangle), \quad (34)$$

and the spatial part of the final atom-pair state $|b^3\Sigma_u^+; R \to \infty\rangle$ is

$$|b^3\Sigma_u^+; R \to \infty\rangle$$
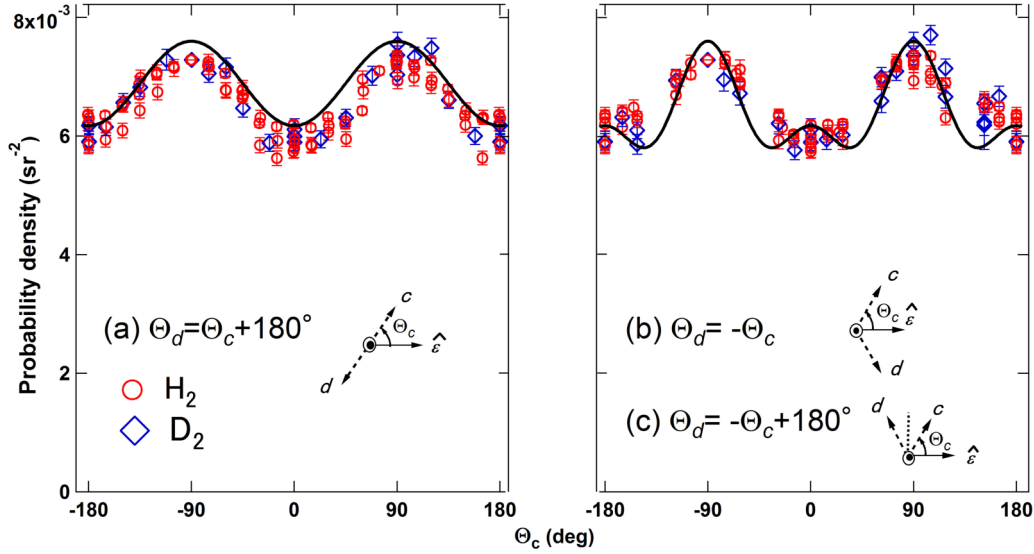$$= (1/\sqrt{2})[|1s^a(1)\rangle\,|1s^b(2)\rangle - |1s^a(2)\rangle\,|1s^b(1)\rangle]. \quad (35)$$

FIG. 9. Comparison between the experimental ACFs of a pair of Lyman-α photons for H$_2$ ($\bigcirc$) and D$_2$ ($\diamond$) in Fig. 5 and the calculated ACF of a pair of Lyman-α photons emitted by the $2p$ atom pairs in the superposition of the $Q_2\,^1\Pi_u(1)$ state and the $Q_2\,^3\Sigma_u^+(2)$ state at infinite internuclear distance (see Sec. IV D for details). The experimental ACFs in Fig. 5 multiplied by 1.15 are shown here since, as mentioned in Sec. III, those values in Fig. 5 have a small uncertainty of a constant multiple in the range 1–1.2. The left panel shows the experimental and theoretical ACFs for the opposite arrangement (a) in Fig. 3, and the right panel shows those for the nonopposite arrangements (b) and (c) because the theoretical ACF for the arrangement (b) is the same as that for the arrangement (c).

The photon-pair state $|\Gamma;\,^1\Pi_u, \eta\rangle$, the spatial part of the other final atom-pair state $|X^1\Sigma_g^+; R \to \infty\rangle$, and its spin part $|\chi_{0\,0}^e\rangle$ are given in Eqs. (16), (17), and (6), respectively. In Eq. (33), the state of the total system $|\Phi; \eta, \eta_{SO}\rangle$ is not separated to the state of the atom pair and that of the photon pair, and we consequently calculate the two-photon correlation function $G^{(2)}(\mathbf{r}_c, t_c, \mathbf{r}_d, t_d)$ for the state $|\Phi; \eta, \eta_{SO}\rangle$ to obtain the ACF for the atom pairs in the $|1_u; \eta, \eta_{SO}, R \to \infty\rangle$ state in Eq. (28).

The ensemble of the atom pairs is, in fact, likely to be a mixed ensemble expressed by the density operator,

$$\rho_a(1_u; \eta_{SO}) = \int_{\eta=0}^{\eta=2\pi} d\eta\, \omega(\eta)$$
$$\times\, |1_u; \eta, \eta_{SO}, R \to \infty\rangle \langle 1_u; \eta, \eta_{SO}, R \to \infty|,$$
(36)

where the population function $\omega(\eta)$ to the $|^1\Pi_u; \eta, R \to \infty\rangle |\chi_{0\,0}^e\rangle$ state given by Eq. (27) is used as is for the population function to the $|1_u; \eta, \eta_{SO}, R \to \infty\rangle$ state since the precursor state of the $2p$ atom pairs in process (1) is the $Q_2\,^1\Pi_u(1)$ state and the contribution of the $Q_2\,^3\Sigma_u^+(2)$ state is negligible in the Franck-Condon region. The ACF for the atom pairs in the $|1_u; \eta, \eta_{SO}, R \to \infty\rangle$ state is thus averaged with the population function, $(1/\pi)\sin^2(\eta/2)$, as well as the distribution of the dissociation direction, $[3/(8\pi)]\sin^2\theta$, which is again based on the fact that the precursor state of the $2p$ atom pairs in process (1) is the $Q_2\,^1\Pi_u(1)$ state and the contribution of the $Q_2\,^3\Sigma_u^+(2)$ state is negligible in the Franck-Condon region. The ACF obtained in this way for the density operator of the atom pairs, $\rho_a(1_u; \eta_{SO})$ in Eq. (36), turns out to be

$$F(\Theta_c, \Phi_c, \Theta_d, \Phi_d; 1_u) = \frac{9}{143\,360\pi^2}\left[\frac{2926}{3} - \frac{70}{3}(\cos 2\Theta_c + \cos 2\Theta_d) + 21[\cos 2(\Theta_c - \Theta_d) + \cos 2(\Theta_c + \Theta_d)]\right.$$
$$+ \frac{112}{3}\cos(\Phi_c - \Phi_d)[\cos 2(\Theta_c - \Theta_d) - \cos 2(\Theta_c + \Theta_d)]$$
$$\left. + \frac{49}{3}\cos 2(\Phi_c - \Phi_d)[2 - 2\cos 2\Theta_c - 2\cos 2\Theta_d + \cos 2(\Theta_c - \Theta_d) + \cos 2(\Theta_c + \Theta_d)]\right], \quad (37)$$

and this ACF is compared with the experimental ACFs of H$_2$ ($\bigcirc$) and D$_2$ ($\diamond$) in Fig. 9 without being convoluted with the present angular resolution. The reason not to be convoluted is that the anisotropy in the theoretical ACF is so weak that the influence of the convolution seems just a little. The left

panel in the figure shows the experimental and theoretical ACFs for the opposite arrangement (a) in Fig. 3, and the right panel shows those for the nonopposite arrangements (b) and (c) because the theoretical ACF, $F(\Theta_c, \Phi_c, \Theta_d, \Phi_d; 1_u)$, for the arrangement (b) is the same as that for the arrangement

(c). The ACF in Eq. (37) is independent of the phase η_{SO}, and it is not hence necessary to calculate the matrix element in Eq. (32). We note that the ACF in Eq. (37) has been normalized according to Eq. (21) and involves no fitting parameter. The experimental ACFs in Fig. 5 are multiplied by 1.15 and the resulting ACFs are shown in Fig. 9 since, as mentioned in Sec. III, the absolute values of the experimental

ACFs have small uncertainty of a constant multiple in the range 1–1.2. It turns out from Fig. 9 that the calculated ACF (the solid line) well reproduces the experimental ACFs of H_2 and D_2 multiplied by 1.15. In conclusion the $2p$ atom pairs in process (1) are approximately expressed by the density operator $\rho_a(1_u; \eta_{SO})$ in Eq. (36), which is explicitly written below,

$$\rho_a(1_u; \eta_{SO}) = \int_{\eta=0}^{\eta=2\pi} d\eta (1/\pi) \sin^2(\eta/2) |1_u; \eta, \eta_{SO}, R \to \infty\rangle \langle 1_u; \eta, \eta_{SO}, R \to \infty|, \tag{38}$$

$$
\begin{aligned}
|1_u; \eta, \eta_{SO}, R \to \infty\rangle = {}& (1/\sqrt{2})\big((1/\sqrt{6})\{-\big[|2p_0^a(1)\rangle|2p_0^b(2)\rangle - |2p_0^a(2)\rangle|2p_0^b(1)\rangle\big] \\
& + \big[|2p_{+1}^a(1)\rangle|2p_{-1}^b(2)\rangle - |2p_{+1}^a(2)\rangle|2p_{-1}^b(1)\rangle + |2p_{-1}^a(1)\rangle|2p_{+1}^b(2)\rangle - |2p_{-1}^a(2)\rangle|2p_{+1}^b(1)\rangle\big]\} \\
& \otimes \{(1/\sqrt{2})[|\alpha(1)\rangle|\alpha(2)\rangle - e^{i\eta}|\beta(1)\rangle|\beta(2)\rangle]\}\big) \\
& - (1/\sqrt{2})e^{-i\eta_{SO}}\big([1/(2\sqrt{2})] \\
& \times \{\big[|2p_{+1}^a(1)\rangle|2p_0^b(2)\rangle + |2p_{+1}^a(2)\rangle|2p_0^b(1)\rangle - |2p_0^a(1)\rangle|2p_{+1}^b(2)\rangle - |2p_0^a(2)\rangle|2p_{+1}^b(1)\rangle\big] \\
& + e^{i\eta}\big[|2p_{-1}^a(1)\rangle|2p_0^b(2)\rangle + |2p_{-1}^a(2)\rangle|2p_0^b(1)\rangle - |2p_0^a(1)\rangle|2p_{-1}^b(2)\rangle - |2p_0^a(2)\rangle|2p_{-1}^b(1)\rangle\big]\} \\
& \otimes \{(1/\sqrt{2})[|\alpha(1)\rangle|\beta(2)\rangle - |\beta(1)\rangle|\alpha(2)\rangle]\}\big),
\end{aligned}
\tag{39}
$$

and the atom-pair state $|1_u; \eta, \eta_{SO}, R \to \infty\rangle$ is entangled because the state of the electron 1 is not definite and the state of the electron 2 is not definite as well, e.g., the projection of the orbital-angular momentum of the electron 1 on the z axis is not definite and that of the electron 2 is not definite as well. We stress that the entanglement in the $2p$ atom pairs originates from the 1_u symmetry properties, which are invariant during the dissociation, and the important role of the 1_u symmetry properties in generating the entanglement is due to the spin-orbit coupling around infinite internuclear distance. An entangled pair of two hydrogen atoms is spontaneously produced through the breakup of a hydrogen molecule because of the invariant symmetry properties.

V. CONCLUSION

We have measured the angular correlation functions (ACFs) of a pair of Lyman-α photons following the photoexcitation to the $Q_2\,^1\Pi_u(1)$ state of H_2 and D_2 with linearly polarized incident light at a 33.66-eV photon energy [see process (1)]. The two photon detectors are placed on the plane perpendicular to the incident light beam. The ACFs for H_2 and D_2 are the same, which shows that the electronic state dominates the state of a pair of two Lyman-α photons and the nuclear motion gives just a small effect. We have identified the electronic state of a pair of $2p$ atoms produced in process (1) in a way that we search for the state of a pair of $2p$ atoms that is reasonably accessed from the precursor $Q_2\,^1\Pi_u(1)$ state in process (1) and gives the ACF in agreement with the experimental ACFs.

The $Q_2\,^1\Pi_u(1)$ state at infinite internuclear distance has turned out not to reproduce the experimental ACFs. We then take account of the nonadiabatic couplings of the $Q_2\,^1\Pi_u(1)$ state with the Q_2 states correlating with

the $n = 2 + n = 2$ dissociation limit, but the consideration of the nonadiabatic couplings does not lead to the identification of the $2p$ atom-pair state in process (1).

It has been found that the spin-orbit coupling plays a significant role at infinite internuclear distance even for H_2 and D_2. Taking the spin-orbit coupling into account and using the two-state approximation and the strong-coupling approximation, we have found out that the 1_u state shown in Eqs. (28) and (39), which is the superposition of the $Q_2\,^1\Pi_u(1)$ state and the $Q_2\,^3\Sigma_u^+(2)$ state due to the spin-orbit coupling, well reproduces the experimental ACFs, and have hence concluded that the $2p$ atom pairs in process (1) are expressed by the density operator in Eqs. (38) and (39) and the $2p$ atom pairs are entangled. We also draw a picture of process (1) that hydrogen molecules are photoexcited to the $Q_2\,^1\Pi_u(1)$ state in the Franck-Condon region and then the $Q_2\,^1\Pi_u(1)$ state comes to superpose with the $Q_2\,^3\Sigma_u^+(2)$ state as the internuclear distance increases to infinity. The superposition is brought about by the spin-orbit coupling, which is effective around infinite internuclear distance because the potential-energy curves of those states approach each other (see Fig. 8), but is negligibly small around the Franck-Condon region because the curves are apart from each other [24]. The entanglement in the $2p$ atom pairs originates from the 1_u symmetry properties of the two-electron system bound by two nuclei, which symmetry properties are invariant during the dissociation, and the important role of the 1_u symmetry properties in generating the entanglement is due to the spin-orbit coupling effective around infinite internuclear distance. In general a breakup of a composite quantum system is likely to result in the spontaneous production of the entangled system of constituents when the composite system has invariant symmetry properties.

[1] M. C. Tichy, F. Mintert, and A. Buchleitner, J. Phys. B **44**, 192001 (2011).

[2] R. Blatt and D. Wineland, Nature (London) **453**, 1008 (2008).

[3] I. Bloch, Nature (London) **453**, 1016 (2008).

[4] H. Miyagi, A. Ichimura, and N. Kouchi, J. Phys. B **40**, 617 (2007).

[5] K. Jänkälä, P. V. Demekhin, S. Heinäsmäki, I. Haar, R. Hentges, and A. Ehresmann, J. Phys. B **43**, 065104 (2010).

[6] J. Robert, F. Zappa, C. R. deCarvalho, G. Jalbert, R. F. Nascimento, A. Trimeche, O. Dulieu, A. Medina, C. Carvalho, and N. V. de Castro Faria, Phys. Rev. Lett. **111**, 183203 (2013).

[7] C. R. de Carvalho, G. Jalbert, F. Impens, J. Robert, A. Medina, F. Zappa, and N. V. De C. Faria, Europhys. Lett. **110**, 50001 (2015).

[8] P. Sancho and L. Plaja, J. Phys. B **42**, 165008 (2009).

[9] T. Tanabe, T. Odagiri, M. Nakano, I. H. Suzuki, and N. Kouchi, Phys. Rev. Lett. **103**, 173002 (2009).

[10] T. Tanabe, T. Odagiri, M. Nakano, Y. Kumagai, I. H. Suzuki, M. Kitajima, and N. Kouchi, Phys. Rev. A **82**, 040101(R) (2010).

[11] Y. Nakanishi, K. Hosaka, R. Kougo, T. Odagiri, M. Nakano, Y. Kumagai, K. Shiino, M. Kitajima, and N. Kouchi, Phys. Rev. A **90**, 043405 (2014).

[12] T. E. Sharp, At. Data Nucl. Data Tables **2**, 119 (1970).

[13] B. H. Bransden and C. J. Joachain, *Physics of Atoms and Molecules* (Prentice-Hall, Englewood Cliffs, NJ, 2003).

[14] T. Odagiri, M. Murata, M. Kato, and N. Kouchi, J. Phys. B **37**, 3909 (2004).

[15] K. Hosaka, K. Shiino, Y. Nakanishi, T. Odagiri, M. Kitajima, and N. Kouchi, Phys. Rev. A **93**, 063423 (2016).

[16] K. Hosaka, Y. Torizuka, P. Schmidt, A. Knie, A. Ehresmann, T. Odagiri, M. Kitajima, and N. Kouchi, Phys. Rev. A **99**, 033423 (2019).

[17] K. Ito, Y. Morioka, M. Ukai, N. Kouchi, Y. Hatano, and T. Hayaishi, Rev. Sci. Instrum. **66**, 2119 (1995).

[18] Y. Hikosaka, T. Aoto, R. I. Hall, and K. Ito, J. Phys. B **36**, 1423 (2003).

[19] T. Aoto, Y. Hikosaka, R. I. Hall, K. Ito, J. Fernández, and F. Martín, Chem. Phys. Lett. **389**, 145 (2004).

[20] K. Amemiya and T. Ohta, J. Synchrotron Radiat. **11**, 171 (2004).

[21] G. Herzberg, *Spectra of Diatomic Molecules, Molecular Spectra, and Molecular Structure* (D. Van Norstrand, Princeton, NJ, 1950), Vol. 1.

[22] J. Tennyson, At. Data Nucl. Data Tables **64**, 253 (1996).

[23] I. Sánchez and F. Martín, J. Chem. Phys. **106**, 7720 (1997).

[24] I. Sánchez and F. Martín, J. Chem. Phys. **110**, 6702 (1999).

[25] F. Martín, J. Phys. B **32**, L181 (1999).

[26] J. Fernández and F. Martín, J. Phys. B **34**, 4141 (2001).

[27] R. N. Zare, Mol. Photochem. **4**, 1 (1972).

[28] Y. V. Vanne, A. Saenz, A. Dalgarno, R. C. Forrey, P. Froelich, and S. Jonsell, Phys. Rev. A **73**, 062706 (2006).

[29] M. O. Scully and M. S. Zubairy, *Quantum Optics* (Cambridge University Press, Cambridge, England, 1997), p. 33.

[30] T. Odagiri, Y. Kumagai, M. Nakano, T. Tanabe, I. H. Suzuki, M. Kitajima, and N. Kouchi, Phys. Rev. A **84**, 053401 (2011).

[31] J. A. Beswick and M. Glass-Maujean, Phys. Rev. A **35**, 3339 (1987).

[32] M. Glass-Maujean and J. A. Beswick, Phys. Rev. A **36**, 1170 (1987).

[33] J. Wang, Q. Meng, and Y. Mo, Phys. Rev. Lett. **119**, 053002 (2017).

[34] P. R. Fontana, Phys. Rev. **125**, 220 (1962).

[35] H. Lefebvre-Brion and R. W. Field, *The Spectra and Dynamics of Diatomic Molecules* (Academic, San Diego, 2004), pp. 180–183.